Control Engineering Practice 165 (2025) 106555

Contents lists available at ScienceDirect

Control Engineering Practice

journal homepage: www.elsevier.com/locate/conengprac

Data-driven controller tuning of hybrid integrator-gain systems for settling time optimization

Jonas G. Hendrikx [a,*], Wouter Weekers [a], Luke F. van Eijk [b,c], Marcel F. Heertjes [a,d], Nathan van de Wouw [a]

[a] Department of Mechanical Engineering, Eindhoven University of Technology, 5600 MB, Eindhoven, The Netherlands
[b] Center of Competency, ASMPT, 6641 TL, Beuningen, The Netherlands
[c] Department of Precision and Microsystems Engineering, Delft University of Technology, 2628 CD, Delft, The Netherlands
[d] Mechatronic Systems Design Department, ASML, 5504 DR, Veldhoven, The Netherlands

ARTICLE INFO

Keywords:
Nonlinear control
Hybrid integrator-gain system (HIGS)
Hybrid control
Data-driven control
Extremum-seeking control (ESC)
Settling time optimization

ABSTRACT

In this work, we present a novel data-driven tuning framework for a class of nonlinear controllers, namely those based on the so-called hybrid integrator-gain system (HIGS). In particular, we focus on minimizing the settling time in point-to-point tasks, i.e., the time required for the error to converge and settle within a desired error bound after the task has finished. The proposed approach is based on sampled-data extremum-seeking control and allows simultaneous tuning of both linear and nonlinear parts of the controller, while guaranteeing input-to-state stability based solely on non-parametric frequency-response function data of the plant. These stability properties are guaranteed by a newly developed procedure for the data-driven verification of existing stability criteria. The efficacy of the proposed approach in tuning HIGS-based controllers for improving the settling time is validated extensively with a case study on an industrial wire bonder showing significant improvements in the worst-case settling time compared to LTI control.

1. Introduction

With the continuously rising demand for high accuracy and increased throughput in many industrial applications, the importance of improving the transient performance of control systems has become more and more evident. For the past decades, linear time-invariant (LTI) control strategies have often been the standard solution in industrial practice. The reason for the widespread use of LTI controllers stems from its low implementation cost, simplicity, predictability regarding stability and performance, and the availability of well-established feedback control methods such as proportional–integral–derivative (PID) control. These well-established methods ensure the existence of intuitive synthesis and tuning techniques widely used in industry, such as manual loop-shaping (Skogestad & Postlethwaite, 2005, Ch. 2), frequency-based auto-tuners (Grassi et al., 2001), and H_∞-design (Zames, 1981). Despite these advantages, LTI controllers have some fundamental limitations leading to design trade-offs that are often undesirable and pose a challenge in high-precision control applications.

One such limitation is Bode's sensitivity integral (Chen, 1995), which states that an increase in error suppression, i.e., a decrease in sensitivity in some frequency range, comes at the cost of error amplification in another range. This limitation is closely coupled with the limitation posed by the Bode gain-phase relation that states that the gain and phase cannot be shaped independently (Freudenberg et al., 2000). Furthermore, in addition to these frequency-domain limitations, a time-domain oriented limitation concerns the trade-off between the rise time and the amount of overshoot of a system's step-response. Numerous nonlinear and/or hybrid control techniques aimed at overcoming these limitations have been proposed. Examples of such control techniques are variable gain control (Hunnekens et al., 2016; Van de Wouw et al., 2008), reset control (Beker et al., 2001; Van Loon et al., 2017; Zhao et al., 2019), nonlinear integrators (Heertjes et al., 2024; Van den Eijnden, Heertjes, Heemels et al., 2020; Van Dinther et al., 2021; Wang et al., 2024), and sliding mode control (Abidi & Sabanovic, 2007).

However, overcoming the limitations of LTI control with nonlinear and/or hybrid control techniques typically comes at the cost of increased design complexity. This increased complexity stems for example from the fact that the superposition principle does not hold for these types of controllers, which means that frequency-domain tuning

* Corresponding author.
E-mail addresses: j.g.hendrikx@tue.nl (J.G. Hendrikx), w.weekers@tue.nl (W. Weekers), luke.van.eijk@asmpt.com (L.F. van Eijk), m.f.heertjes@tue.nl (M.F. Heertjes), n.v.d.wouw@tue.nl (N. van de Wouw).

https://doi.org/10.1016/j.conengprac.2025.106555
Received 31 January 2025; Received in revised form 17 July 2025; Accepted 20 August 2025
Available online 17 September 2025

as common in well-established LTI design approaches is generically not applicable. As a result, the design of nonlinear and/or hybrid controllers is often time-consuming and requires a high level of control engineering expertise. This limits the widespread adoption of such controllers, especially in industrial applications where high throughput and accuracy demands necessitate tuning on an individual machine basis, e.g., to account for possible machine-to-machine variations.

Data-driven tuning approaches potentially allow overcoming the time-consuming nature of and need for expertise in controller design by updating controller parameters based solely on measured performance data. Examples of such approaches include extremum seeking control (ESC) (Ariyur & Krstic, 2003; Khong, Nešić, Tan et al., 2013), iterative feedback tuning (IFT) (Hjalmarsson et al., 1998), and iterative learning control (ILC) (Ahn et al., 2007). However, a challenge in using these approaches for the design of nonlinear and/or hybrid feedback controllers arises from the absence of closed-loop stability guarantees in IFT and ESC, which are crucial in feedback control design, whereas ILC mostly addresses feedforward design. Therefore, the goal of this work is to develop a data-driven tuning algorithm for nonlinear and/or hybrid controllers, optimizing settling performance while warranting closed-loop stability.

In particular, we focus on controllers containing a hybrid integrator-gain system (HIGS) (Deenen et al., 2017). HIGS controllers have shown the ability to address the inherent limitations of LTI controllers in terms of transient performance, as proven by Van den Eijnden, Heertjes, Heemels et al. (2020). Additionally, they benefit from the availability of tools to verify whether the system is input-to-state stable (ISS), even in the presence of multiplicative plant uncertainties, based solely on (measured) frequency-response function (FRF) data of the plant (Van den Eijnden, 2022; Van den Eijnden et al., 2024, Ch. 4). The existence of such tools is crucial in tuning for machine-to-machine variation, as it allows for stability guarantees without the need for a detailed parametric model of the plant.

The three main contributions of this paper are therefore as follows. The first contribution is the development of a framework that facilitates data-driven tuning of HIGS-based controllers to optimize transient system performance characterized by the settling time. In contrast to the approach presented by Heertjes et al. (2019) for data-driven tuning of a HIGS, the proposed approach allows simultaneous tuning of both the HIGS parameters and the linear part of the HIGS-based controller. The second contribution is the development of an automated, data-driven stability check for HIGS-based controllers, based on the frequency-domain conditions derived in Van den Eijnden et al. (2024), which solely requires (measured) FRF data of the plant. This stability check can be used to provide guarantees on input-to-state stability of the system in data-driven tuning frameworks. The third contribution is a case study on an industrial wire bonder system used in the semiconductor industry, showcasing the real-world applicability of the proposed tuning approach in tuning input-to-state stable HIGS-based controllers for improved transient performance.

The remainder of this paper is organized as follows. In Section 2, we describe how HIGS-based controllers can be constructed and formulate the transient performance optimization problem that we aim to solve. In Section 3, we present the developed automated, data-driven stability check and the proposed approach to solve the transient performance optimization problem. The results of the industrial case study are presented in Section 4, and concluding remarks are given in Section 5.

2. System description and problem formulation

In this section, we first describe the design of HIGS-based controllers and discuss existing frequency-domain conditions based on (measured) FRF data that can be used to verify whether the closed-loop system is ISS. Next, we introduce the transient performance optimization problem that we aim to solve.

2.1. HIGS-based controller design

The HIGS is a nonlinear control element first introduced by Deenen et al. (2017) and is inspired by the Clegg integrator (Clegg, 1958). It is mathematically defined as the piecewise-linear system (see, e.g., Van den Eijnden et al. (2024)):

$$\mathcal{H}: \begin{cases} \dot{x}_h(t) = \omega_h z(t), & \text{if } (z(t), u(t), \dot{z}(t)) \in \mathcal{F}_1, \\ x_h(t) = k_h z(t), & \text{if } (z(t), u(t), \dot{z}(t)) \in \mathcal{F}_2, \\ u(t) = x_h(t) \end{cases} \tag{1}$$

with state $x_h(t) \in \mathbb{R}$, input $z(t) \in \mathbb{R}$, and output $u(t) \in \mathbb{R}$ at time $t \geq 0$. Two operating modes can be recognized in (1). In the first mode, the integrator mode active in the set $\mathcal{F}_1 := \{(z,u,\dot{z}) \in \mathbb{R}^3 \mid k_h z u \geq u^2 \wedge (z,u,\dot{z}) \notin \mathcal{F}_2\}$, the HIGS behaves like a linear integrator with integrator frequency $\omega_h \in \mathbb{R}_{>0}$. In the second mode, the gain mode active in the set $\mathcal{F}_2 := \{(z,u,\dot{z}) \in \mathbb{R}^3 \mid u = k_h z \wedge \omega_h z^2 > k_h \dot{z} z\}$, the HIGS represents a static gain $k_h \in \mathbb{R}_{>0}$. The sets $\mathcal{F}_1$ and $\mathcal{F}_2$ are constructed as to keep the input–output pair (z,u) contained in the $[0, k_h]$-sector defined by $\mathcal{F} := \{(z,u,\dot{z}) \in \mathbb{R}^3 \mid k_h z u \geq u^2\} = \mathcal{F}_1 \cup \mathcal{F}_2$ (see, e.g., Deenen et al. (2017)), which ensures that the sign of u remains aligned with the sign of z; similar to the Clegg integrator (Clegg, 1958) described by (see, e.g., Zaccarian et al. (2005))

$$\mathcal{R}: \begin{cases} \dot{x}_r(t) = \omega_r z(t), & \text{if } z(t)u_r(t) \geq 0, \\ x_r\left(t^+\right) = 0, & \text{if } z(t)u_r(t) \leq 0, \\ u_r(t) = x_r(t) \end{cases} \tag{2}$$

with state $x_r(t) \in \mathbb{R}$, input $z(t) \in \mathbb{R}$, output $u_r(t) \in \mathbb{R}$, and integrator frequency $\omega_r \in \mathbb{R}_{>0}$. In the Clegg integrator, the output is reset to zero when a sign change of its input is detected, which potentially causes excitation of lightly-damped plant resonances. In contrast, the two operating modes of the HIGS in (1) ensure the signs of u and z remain aligned while also ensuring that u remains continuous, which reduces such detrimental excitation.

The difference between the Clegg integrator and the HIGS is illustrated by their time responses subject to a sinusoidal input $z(t) = \sin(\omega t)$ with $\omega = 1$ rad/s in Fig. 1. Initially, the responses of both the Clegg integrator and the HIGS are identical to the response of a linear integrator. However, the responses start to deviate when the HIGS switches to the gain mode when its output u equals the scaled input $k_h z$, at around $t \approx 0.7\pi/\omega$ in Fig. 1. This switch to the gain-mode causes the zero crossing of the output of the HIGS to occur at the same time as the zero crossing of its input, while the output of a linear integrator would lag 90 degrees behind its input, leading to a reduction in phase lag for the HIGS compared to a linear integrator. Note that such a reduction in phase lag can potentially aid in reducing overshoot and settling time of the transient response (Van den Eijnden, Heertjes, Heemels et al., 2020; Van Dinther et al., 2021). Fig. 1 also shows how a similar reduction in phase lag is obtained for the Clegg integrator by a hard reset of its output to zero at $t = \pi/\omega$.

It is useful to analyze the (approximate) frequency-domain characteristics of the HIGS to understand how to take advantage of this reduction in phase lag. This approximate analysis can be performed using the so-called describing function $D_{\mathcal{H}}(\omega)$ of the HIGS (Van den Eijnden, Heertjes, Heemels et al., 2020), which describes the relation between harmonic excitation of the HIGS input z and the first harmonic of the HIGS output u. This describing function is given by

$$D_{\mathcal{H}}(\omega) = \frac{\omega_h}{j\omega}\left(\frac{\gamma(\omega)}{\pi} + j\frac{e^{-2j\gamma(\omega)} - 4e^{-j\gamma(\omega)} + 3}{2\pi}\right) + k_h\left(\frac{\pi - \gamma(\omega)}{\pi} + j\frac{e^{-2j\gamma(\omega)} - 1}{2\pi}\right) \tag{3}$$

with $\gamma(\omega) = 2\arctan(k_h\omega/\omega_h)$, which follows for example from Heertjes et al. (2019, Eqs. (13) and (14)) using Euler's formula. Plotting the magnitude- and phase-characteristics of (3) shows that the HIGS has approximate magnitude characteristics similar to those of a linear low-pass filter, as illustrated in Fig. 2, with asymptotes $\lim_{\omega\to 0} D_{\mathcal{H}}(\omega) = k_h$

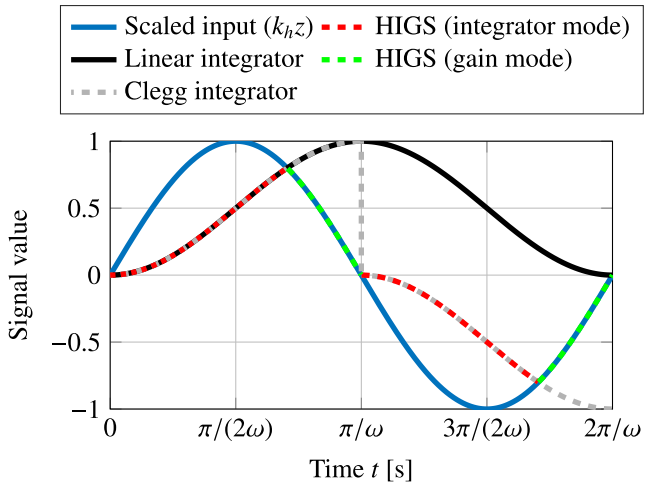

Fig. 1. Comparison of time responses of a linear integrator, a Clegg integrator, and the HIGS, for a sinusoidal input $z(t) = \sin(\omega t)$ with $\omega = 1$ rad/s, $\omega_r = \omega_h = 0.5\omega$, and $k_h = 1$. While both the Clegg integrator and the HIGS keep the sign of their outputs aligned with the sign of their inputs to reduce their phase lag compared to a linear integrator, the HIGS does so in a continuous fashion instead of via a hard reset for the Clegg integrator.

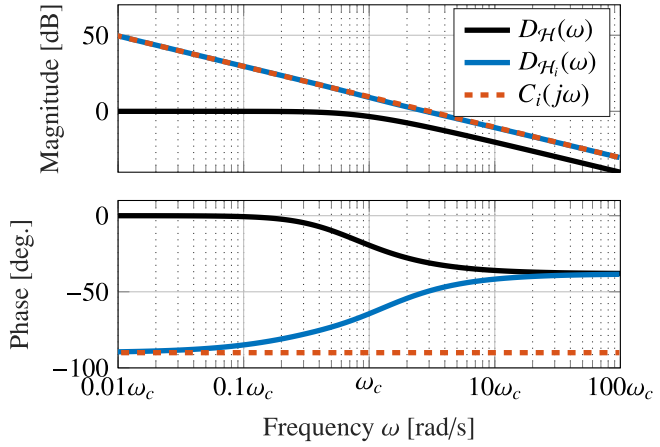

Fig. 2. Comparison of the magnitude and phase characteristics of the describing function $D_{\mathcal{H}}(\omega)$ in (3), the describing function $D_{\mathcal{H}_i}(\omega)$ of a HIGS-based integrator $\mathcal{H}_i$ ($\omega_h = 200\pi$ rad/s and $k_h = 1$), and a linear integrator $C_i(s)$ ($\omega_i = 3\omega_c$). While the magnitude characteristics of $D_{\mathcal{H}_i}$ and C_i are similar, $D_{\mathcal{H}_i}$ shows a significant reduction in phase lag.

and $\lim_{\omega\to\infty} D_{\mathcal{H}}(\omega) = \omega_h(1+4j/\pi)/(j\omega)$. However, in contrast to a linear low-pass filter, $D_{\mathcal{H}}$ only shows a phase lag of around 38 degrees, instead of 90 degrees.

An example of how this reduction in phase lag can be exploited in control design is by using quasi-linear reasoning to design a HIGS-based version of a given LTI controller C^* based on the describing function in (3). To this end, we adopt ideas proposed in Van den Eijnden, Heertjes, Heemels et al. (2020) and Van den Eijnden, Heertjes, Nijmeijer (2020): we place the HIGS in front of the LTI filter C^* and pre-filter the input to the HIGS with an LTI filter H^{-1} aimed at 'compensating' the magnitude characteristics of (3). Given the aforementioned approximate magnitude characteristics of the HIGS, we choose the transfer function $H(s)$ as

$$H(s) = k_h\left(\frac{\omega_c}{s+\omega_c}\right) \tag{4}$$

with $\omega_c = |1 + (4j/\pi)|\omega_h/k_h$ rad/s the crossover frequency (i.e., the point where the aforementioned asymptotes of the magnitude characteristics cross) and $s \in \mathbb{C}$ the Laplace variable. This causes H to have similar magnitude characteristics as (3). As a result, the pre-filter H^{-1} thus compensates for the (approximate) magnitude characteristics of the HIGS, and provides an additional phase lead, while post-filtering the HIGS output by C^* serves to shape the overall magnitude characteristics to be similar to those of the LTI controller C^*. Note that for practical implementation of the non-proper filter H^{-1}, its transfer function can be multiplied by $(\epsilon s + 1)^{-1}$ with $\epsilon > 0$ small, while in addition multiplying the transfer function of C^* with $(\epsilon s + 1)$ to not change the overall frequency characteristics of the describing function. To illustrate the resulting phase benefits of the HIGS-based control element, consider the case where the LTI filter C^* is a linear integrator with the transfer function $C_i(s) = \omega_i/s$ with integrator frequency $\omega_i \in \mathbb{R}_{>0}$, resulting in a HIGS-based integrator $\mathcal{H}_i$. Comparing the magnitude and phase characteristics of the describing function

$$D_{\mathcal{H}_i}(\omega) = H^{-1}(j\omega)D_{\mathcal{H}}(\omega)C_i(j\omega) \tag{5}$$

of $\mathcal{H}_i$ to those of a linear integrator shows that the magnitude responses are similar, while the phase lag is reduced from 90 degrees for the linear integrator to 38 degrees for $D_{\mathcal{H}_i}$ for frequencies sufficiently higher than ω_c, as shown in Fig. 2.

Despite the usefulness of the describing function in an analysis of the controller structure, it is important to note that the exclusive reliance on the first harmonic overlooks the effect of higher-order harmonics (Van Eijk et al., 2023). The exclusion of higher-order harmonics, in combination with the lack of the superposition principle, means that the describing function provides an incomplete representation of the true response. It is therefore crucial to recognize these limitations when employing the describing function for analysis or controller design. This limitation also means that a frequency-based tuning approach based on the describing function might result in suboptimal performance, which once more motivates a time-domain tuning approach as we present in Section 3.

2.2. Pre- and post-filtering

The lack of the superposition principle due to the nonlinear nature of the HIGS potentially introduces undesirable effects caused by input-dependent phenomena. One such undesirable effect happens for example when a high-frequency component with a relatively large amplitude is present next to a low-frequency component, as illustrated in Fig. 3. This high-frequency component in the input induces high-frequency switching behavior of the HIGS, which reduces the amplitude of the HIGS output (Chu et al., 2024; Heertjes et al., 2021). This reduced amplitude, in turn, translates to a decrease in effective gain, leading to compromised disturbance rejection capability of the low-frequency component in the input. To prevent this rapid switching, an LTI frequency lifting pre-filter W can be introduced before the HIGS to reduce (unwanted) frequency content in the input to the HIGS (see Fig. 3), while its inverse W^{-1} is used as a post-filter to compensate for the magnitude and phase characteristics of W (Heertjes et al., 2009, 2021). Possible design choices for W include notch filters, low-pass filters, and bandpass filters. By including these frequency lifting filters, the final HIGS-based version $\mathcal{H}_*$ of an LTI controller C^* is obtained as illustrated in Fig. 4. Note that by combining the lifting filter W with its inverse, their effect is not visible in the describing-function-based frequency-domain characteristics of the HIGS-based controller $\mathcal{H}_*$, as their frequency-domain characteristics cancel out. Consequently, the tuning of this lifting filter using the describing function in (3) is impossible, motivating a time-domain tuning framework. Furthermore, we care to stress that the controller structure in Fig. 4 is just one of possibly many ways in which the HIGS can be used in control design, and that the question which controller structure leads to the best performance is still an open research question that is outside the scope of this work, which focusses on data-driven controller tuning for a given structure.

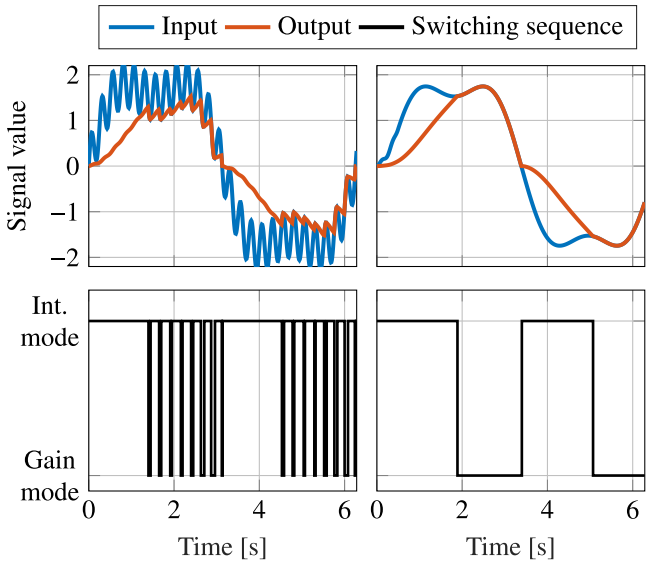

Fig. 3. Scaled HIGS response with HIGS parameters $\omega_h = 1$ and $k_h = 1.5$, and scaling factor $1/k_h$ (top), and switching behavior (bottom) without lifting filter W (left) and with lifting filter W (right). The input signal is the sinusoidal signal $z(t) = 2\sin(t) + 0.5\sin(3t) + 0.5\sin(8\pi t)$. Filtering out the high-frequency component prevents rapid switching of the HIGS, resulting in an increased effective gain.

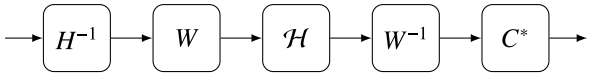

Fig. 4. Illustration of a HIGS-based version $\mathcal{H}_*$ of an LTI controller C^*, including a frequency lifting filter W.

2.3. Frequency-domain conditions for stability

Input-to-state stability (Sontag & Wang, 1995, Definition 2.1) of the closed-loop system is important for the successful application of HIGS-based controllers. Therefore, consider a closed-loop system consisting of a plant P and a HIGS-based feedback controller $\mathcal{H}_*$ as discussed in the previous section. Let G be a generalized plant consisting of all LTI components of this closed-loop system, with input channels $w := [\theta^T\ r]^T$ and u, and output channel y, as illustrated in Fig. 5 (an example of G will be given in the industrial case study in Section 4). We describe this generalized plant using the minimal state-space representation

$$G: \begin{cases} \dot{x}_g(t) = A_g x_g(t) + B_g u(t) + B_w w(t), \\ y(t) = C_g x_g(t) \end{cases} \tag{6}$$

with state vector $x_g(t) \in \mathbb{R}^{n_x}$. Furthermore, we denote the transfer functions from u to y and from w to y as

$$\begin{bmatrix} G_{yu}(s) & G_{yw}(s) \end{bmatrix} = C_g(sI - A_g)^{-1}\begin{bmatrix} B_g & B_w \end{bmatrix}. \tag{7}$$

A sufficient frequency-domain condition to guarantee that the feedback interconnection of the generalized plant G and the HIGS $\mathcal{H}$ is ISS is derived by Van den Eijnden et al. (2024) and given by the following theorem.

Theorem 1. *Suppose that the matrix $A_g - k_h B_g C_g$ is Hurwitz. If there exist parameters $\lambda \geq 0$ and $k \geq 1$, such that, for all $\omega \in \mathbb{R} \cup \{\infty\}$, the frequency-domain inequality*

$$1 + X(\omega, k) - \lambda Y(\omega, k) > 0 \tag{8}$$

is satisfied, where

$$X(\omega, k) = \mathrm{Re}\left\{ \left((\omega_h - k_h j\omega) S(j\omega) - k\frac{\omega_h}{k_h} \right) L(j\omega) \right\}, \tag{9}$$

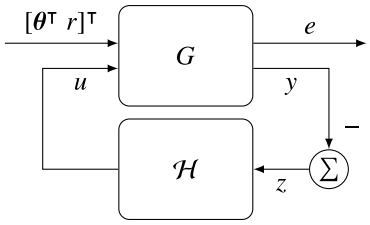

Fig. 5. Feedback interconnection of a generalized plant G consisting of all LTI components in the closed-loop system, and the HIGS $\mathcal{H}$.

$$Y(\omega, k) = \mathrm{Re}\left\{ \left(k k_h S(j\omega) + (1 - k) \right) L(j\omega) \right\} \tag{10}$$

with $S(j\omega) := G_{yu}(j\omega)\left(1 + k_h G_{yu}(j\omega)\right)^{-1}$ and $L(j\omega) := \left(j\omega + k\omega_h/k_h\right)^{-1}$, then the overall closed-loop system shown in Fig. 5 is ISS.

As remarked in Van den Eijnden et al. (2024), checking whether the matrix $A_g - k_h B_g C_g$ is Hurwitz can be done by counting the number of times the Nyquist contour of the open-loop characteristics with the HIGS in the gain mode, i.e., the Nyquist contour of $k_h G_{yu}(j\omega)$, encircles the critical point $(-1, 0)$ (Franklin et al., 2015, Sec. 6.3). Furthermore, satisfaction of (8) can be verified graphically by checking whether the (X, Y)-curve lies fully to the right of the line $1 + X - \lambda Y = 0$ in a Popov-like plot. This is illustrated in Fig. 6, where the dashed line denotes $1 + X - \lambda Y = 0$, and the colored lines denote the (X, Y)-curve for various values of k. In this figure, (8) holds for $k = k_2$ since the orange curve is fully to the right of the dashed line.

However, while Fig. 6 illustrates that satisfaction of (8) can easily be checked graphically for given values of λ and k, verifying automatically whether there exist $\lambda \geq 0$ and $k \geq 1$ for which (8) is satisfied is not a trivial task. Since in an automated tuning framework for HIGS-based controllers it needs to be verified automatically if the closed-loop system is ISS, we therefore present in Section 3.1 a novel automated approach to verify whether the conditions of Theorem 1 are satisfied.

2.4. Performance optimization problem formulation

Let $C\{\mathcal{H}\}$ denote a controller consisting of a HIGS-based element $\mathcal{H}_*$ as in Fig. 4, and in addition possibly some other LTI filters (an example will be given in the industrial case study in Section 4). By parametrizing $C\{\mathcal{H}\}$ with tunable parameters $\theta \in \mathbb{R}^{n_\theta}$, and using it as a feedback controller for an LTI plant P to track a time-varying reference profile $r(t) \in \mathbb{R}$, we obtain a multi-input-single-output system Σ with inputs $r(t)$ and θ, and error output $e(t, \theta) \in \mathbb{R}$, as illustrated in Fig. 7. Here, $e(t, \theta) := r(t) - y_p(t, \theta)$, with $y_p(t, \theta) \in \mathbb{R}$ the output of the plant P, denotes the tracking error resulting from tracking the reference $r(t)$. We task this closed-loop system Σ with performing point-to-point tasks from an initial plant output r_0 to a desired (constant) plant output r_d. The total duration T of each point-to-point task is at least the sum of the tracking time t_r, the settling time $t_s(\theta)$, and the action time t_a. The tracking time t_r is the time required by the reference to transition from r_0 to r_d. Ideally, the plant output $y_p(t, \theta)$ remains constant at the desired output r_d at $t = t_r$, however, in general, some transient response remains. This transient response converges, until the absolute value of the tracking error $e(t, \theta)$ remains within a desired error bound e_b. The time required before the error no longer violates the error bound after $t = t_r$ constitutes the settling time $t_s(\theta)$, i.e.,

$$t_s(\theta) := \min_{\tau \in [0, T - t_r]} \tau \tag{11a}$$

$$\text{s.t. } |e(t, \theta)| \leq e_b\ \forall t \in [t_r + \tau, T]. \tag{11b}$$

The action time t_a is the time required to perform a given action after the error has settled, e.g., to perform a machine operation that requires the level of accuracy specified by the error bound e_b. Given the high throughput demands in industrial applications, it is desired to choose

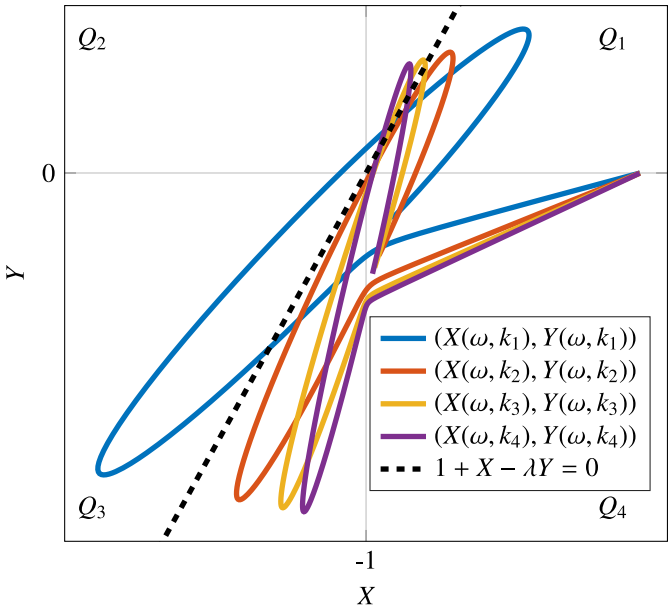

Fig. 6. Illustration of the Popov-like plot that can be used to verify satisfaction of (8) graphically. The different colors illustrate that (8) is satisfied for $k = k_2$, since the orange (X,Y)-curve is fully to the right of the dashed line. (For interpretation of the references to color in this figure legend, the reader is referred to the web version of this article.)

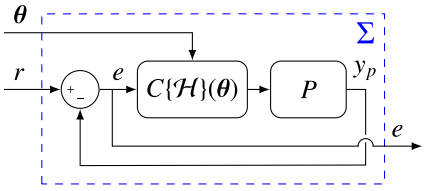

Fig. 7. Block scheme illustrating the feedback interconnection of a HIGS-based controller $C\{\mathcal{H}\}$ parametrized by tunable parameters θ, and an LTI plant P, resulting in a closed-loop multi-input-single-output system Σ with inputs $r(t)$ and θ, and output $e(t,\theta)$.

T as small as possible. Since T must be at least the sum of t_r, $t_s(\theta)$, and t_a, i.e., $T \geq t_r + t_s(\theta) + t_a$, and since t_a is typically fixed due to the to-be-performed action, one can optimize either the reference $r(t)$ or minimize the settling time $t_s(\theta)$. In this work, we assume the reference $r(t)$ to be predefined, and hence aim to minimize the settling time $t_s(\theta)$. That is, we aim to solve the following optimization problem

$$t_s^* := \min_{\theta\in\Theta} t_s(\theta), \tag{12}$$

where Θ denotes the set of all parameter combinations for which the closed-loop system Σ is ISS with respect to the reference $r(t)$. Note that a subset of this set can be characterized by the conditions in Theorem 1.

Solving (12) directly, however, is challenging due to the discontinuous dependence of $t_s(\theta)$ on θ. This discontinuous nature of $t_s(\theta)$ means that small changes in θ can lead to large changes in the settling time, as illustrated in Weekers et al. (2025). To circumvent this extreme sensitivity of the settling time to changes in θ when solving (12), a problem reformulation was proposed in Weekers et al. (2025) in which (12) is reformulated as a cascade of two optimization problems with continuous cost functions. While the continuous nature of the cost functions in this reformulation facilitated devising a solution strategy for solving (12), the method devised in Weekers et al. (2025) only considers LTI controllers. The main limitation challenging a natural extension of the work of Weekers et al. (2025) to HIGS-based controllers is the reliance on the Nyquist stability criterion to guarantee stability of the closed-loop system between iterations of the optimization algorithm based on (measured) FRF data of the plant. Due to the inherent nonlinear nature of HIGS-based controllers, closed-loop stability properties cannot be guaranteed on the basis of such a traditional frequency-domain tool for LTI controllers alone. Therefore, in the next section, we develop a solution strategy inspired by the solution strategy in Weekers et al. (2025) for solving (12) when there is a HIGS element in the system.

3. A data-driven tuning framework for HIGS-based controllers

In this section, we present a novel automated procedure for verifying the stability conditions outlined in Theorem 1. Subsequently, we present our approach for solving (12) that includes this automated procedure.

3.1. Automated, data-driven verification of stability conditions

To verify the conditions of Theorem 1 in an automated framework, we assume that (i) (measured) data of $G_{yu}(j\omega)$ is available for a sufficiently wide range of frequencies, (ii) the frequency resolution of the data is sufficiently high, (iii) the number of integrators in G_{yu} is known, and (iv) $G_{yu}(j\omega) \to 0$ as $\omega \to \infty$. As mentioned before, checking whether the matrix $A_g - k_h B_g C_g$ is Hurwitz is then relatively straightforward. Namely, by drawing the Nyquist contour of $k_h G_{yu}(j\omega)$ based on (measured) frequency-response data and interpolating between data points, the number of up- and downward crossings of the negative real axis to the left of the critical point $(-1,0)$ can be determined. The net number of downward crossings corresponds to the number of times the critical point is encircled in the counterclockwise direction, which allows drawing conclusions about stability (see, e.g, Franklin et al. (2015, Sec. 6.3)) of the feedback interconnection of the generalized plant G and the HIGS $\mathcal{H}$ with the HIGS in gain mode.

If the matrix $A_g - k_h B_g C_g$ is Hurwitz, it remains to be verified whether there exist constants $\lambda \geq 0$ and $k \geq 1$ such that (8) is satisfied. Verification of the conditions in Theorem 1 can be simplified by recognizing that $X(\omega,k)$ and $Y(\omega,k)$ in (9) and (10) are independent of λ, leaving λ as a free variable to satisfy (8). Furthermore, note that $\arctan(1/\lambda)$ is the positive angle between the horizontal axis and the line $1 + X - \lambda Y = 0$, showing that decreasing λ to zero results in a vertical line, and increasing λ to ∞ corresponds to a horizontal line. Consequently, for any given value of k, the (X,Y)-curve is fully to the right of the line $1 + X - \lambda Y = 0$ if the largest angle that the lines connecting the point $(-1,0)$ to points on the curve make with the horizontal axis is (i) smaller than $\pi/2$ and (ii) smaller than the smallest angle plus π. Since (8) is satisfied if the (X,Y)-curve is fully to the right of the line $1 + X - \lambda Y = 0$, it thus remains to verify for a given value of k whether there exists a $\lambda \geq 0$ such that this is indeed the case. To this end, let

$$\phi(\omega,k) := \arctan\left(\frac{Y(\omega,k)}{X(\omega,k)+1}\right) \tag{13}$$

denote the angle between the horizontal axis and the line connecting $(X(\omega,k),Y(\omega,k))$ to the point $(-1,0)$. Then, verifying whether there exists a $\lambda \geq 0$ such that (8) is satisfied for a given value of k thus amounts to verifying whether

$$\max_{\omega\in\mathbb{R}} \phi(\omega,k) < \min\left\{\frac{\pi}{2}, \min_{\omega\in\mathbb{R}}(\phi(\omega,k)+\pi)\right\}. \tag{14}$$

While (14) simplifies verifying whether a $\lambda \geq 0$ exists for a given value of k to verifying satisfaction of a single inequality, checking it for many values of $k \geq 1$ is still computationally expensive. In addition, depending on the frequency resolution of the frequency-response data, the number of times (13) needs to be evaluated can be large, meaning that verifying (14) for many values of k can be both computationally expensive and time-consuming. However, the following observations

can be made to reduce the computational burden for a given value of k. Define

$$\mathcal{P} := \{(X(\omega_1,k),Y(\omega_1,k)),\dots,(X(\omega_{N_\omega},k),Y(\omega_{N_\omega},k))\} \tag{15}$$

with ω_j, $j = 1,2,\dots,N_\omega$, the frequencies for which the frequency response has been measured/constructed. Furthermore, let

$$Q_1 := \{(X,Y)\in\mathbb{R}^2 \mid X > -1, Y > 0\}, \tag{16}$$

$$Q_2 := \{(X,Y)\in\mathbb{R}^2 \mid X \le -1, Y \ge 0\}, \tag{17}$$

$$Q_3 := \{(X,Y)\in\mathbb{R}^2 \mid X < -1, Y < 0\}, \tag{18}$$

denote, respectively, the first, second and third quadrant around the point $(-1,0)$ of the Popov-like plot as illustrated in Fig. 6. Clearly, if any of the points in $\mathcal{P}$ lies in Q_2, there exists no $\lambda \ge 0$ such that (8) is satisfied, i.e., (14) is not satisfied for a given value of k if $\mathcal{P}\cap Q_2 \neq \emptyset$ for that value of k. Furthermore, (14) trivially holds for a given value of k if either $\mathcal{P}\cap(Q_1\cup Q_2)=\emptyset$ or $\mathcal{P}\cap(Q_2\cup Q_3)=\emptyset$ for that value of k, since in these cases all points are below/to the right of the lines $Y=0$ and $X=-1$, respectively. Finally, if none of these previous conditions hold, it holds that $\mathcal{P}\cap Q_2=\emptyset$, $\mathcal{P}\cap Q_1\neq\emptyset$, and $\mathcal{P}\cap Q_3\neq\emptyset$. Hence, the point on the (X,Y)-contour corresponding to the largest angle $\phi(\omega,k)$ is contained in Q_1, while the point on the (X,Y)-contour corresponding to the smallest angle $\phi(\omega,k)$ is contained in Q_3. Therefore, in this case, it suffices to determine the largest angle

$$\phi_{\max} := \max_{\omega\in\mathbb{R}} \phi(\omega,k) \tag{19a}$$

$$\text{s.t. } (X(\omega,k),Y(\omega,k)) \in \mathcal{P}\cap Q_1 \tag{19b}$$

of the lines connecting the point $(-1,0)$ to any of the points in Q_1, and the smallest angle

$$\phi_{\min} := \min_{\omega\in\mathbb{R}} \phi(\omega,k) \tag{20a}$$

$$\text{s.t. } (X(\omega,k),Y(\omega,k)) \in \mathcal{P}\cap Q_3 \tag{20b}$$

of the lines connecting the point $(-1,0)$ to any point in Q_3, and to verify whether $\phi_{\max} < \phi_{\min}+\pi$ to verify if (14) is satisfied. In our experience, this approach results in a significant reduction of the computational burden, as $\mathcal{P}\cap Q_2\neq\emptyset$ for many values of k.

With the above approach for verifying for given values of k whether there exists a $\lambda\ge 0$ such that (8) is satisfied, it remains to be verified if there exists a $k\ge 1$ such that these conditions are satisfied. To this end, we adopt an iterative approach in which k is incremented by a fixed value Δk, starting from $k=1$, and the above procedure for verifying satisfaction of (14) for the current value of k is performed until either (14) is satisfied or k reaches a specified upper bound $\bar{k}$. The resulting algorithm for verifying satisfaction of the conditions of Theorem 1 is given in Algorithm 1. Note that iterating over values of k may introduce some additional conservativeness to the sufficient conditions from Theorem 1 for guaranteeing that the feedback interconnection of G and $\mathcal{H}$ is ISS. For example, choosing the increment Δk too large or the upper bound $\bar{k}$ too small might result in failure of finding a value of k for which the conditions are satisfied even if such a k exists.

Remark 1. In Van den Eijnden (2022, Sec. 4.4), an extension of the frequency-domain conditions discussed in Section 2.3 for verifying input-to-state stability of the closed-loop system is provided, which allows taking multiplicative plant uncertainties in G_{yu} into account. This extension amounts to

(i) checking whether the matrix $A_g - k_h B_g C_g$ is Hurwitz;

(ii) checking whether the matrix $A_g - k_h B_g C_g$ is also Hurwitz for all possible realizations of the uncertainty, by checking whether

$$\|k_h \widetilde{W}(j\omega) G_0(j\omega)\| < \|1 + k_h G_0(j\omega)\| \quad \forall\omega\in\mathbb{R} \tag{21}$$

with $\widetilde{W}$ a stable and proper weighting filter that captures magnitude information about the uncertainty and $G_0(j\omega)$ the nominal frequency-domain characteristics of G_{yu};

(iii) drawing uncertainty ellipses around the (X,Y)-contour (cf. Van den Eijnden (2022, Eq. (4.48))) and verifying whether the hull of those ellipses is fully to the right of the line $1+X+\lambda Y=0$.

Note that our procedure in Algorithm 1, with some slight modifications, can also be used to perform these three tasks. First, (i) can be performed by replacing the open-loop characteristics $G_{yu}(j\omega)$ in lines 2–4 of Algorithm 1 by the nominal open-loop characteristics $G_0(j\omega)$. Next, for (ii), it can be verified whether the inequality in (21) is satisfied for frequencies $\omega_1,\dots,\omega_{N_\omega}$ for which the frequency response $G_0(j\omega)$ has been measured/constructed. Under the assumptions mentioned at the beginning of this section, this gives a good indication whether (21) is satisfied for all $\omega\in\mathbb{R}$. Finally, (iii) can be performed by constructing each uncertainty ellipse using $N_{ellipse}$ equally spaced points (with $N_{ellipse}$ sufficiently large), and changing $\mathcal{P}$ in (15) to

$$\mathcal{P} = \cup_{i=1,\dots,N_{ellipse}} \{(X_i(\omega_1,k),Y_i(\omega_1,k)),\dots, (X_i(\omega_{N_\omega},k),Y_i(\omega_{N_\omega},k))\}. \tag{22}$$

Here, $X_i(\omega,k)$ and $Y_i(\omega,k)$ denote, respectively, the x- and y-coordinates of the ith point on the uncertainty ellipse around the point $(X(\omega,k), Y(\omega,k))$.

Algorithm 1: Data-driven verification of the conditions of Theorem 1.

Input: HIGS gain k_h, HIGS integrator frequency ω_h, open-loop characteristics $G_{yu}(j\omega)$, process sensitivity with HIGS in gain mode $S(j\omega)$, $\mathcal{P}$ as in (15), increment Δk, upper bound $\bar{k}$

Output: `ISSguaranteed`

1: $k \leftarrow 1$, `ISSguaranteed` $\leftarrow$ **false**
2: By counting the number and direction of sign changes, determine the number of times the Nyquist contour of $k_h G_{yu}(j\omega)$ crosses the negative real axis to the left of $(-1,0)$ in the up- and downward directions.
3: Determine the net number of times the point $(-1,0)$ is encircled in the counterclockwise direction by subtracting the number of upward crossings from the number of downward crossings.
4: Based on the number of times the point $(-1,0)$ is encircled in counterclockwise direction, conclude whether the matrix $A_g - k_h B_g C_g$ is Hurwitz (see, e.g., (Franklin et al., 2015, Sec. 6.3)).
5: **if** the matrix $A_g - k_h B_g C_g$ is Hurwitz **then**
6: **while** $k < \bar{k}$ **and not** `ISSguaranteed` **do**
7: **if** $\mathcal{P}\cap Q_2 = \emptyset$ **then**
8: **if** $\mathcal{P}\cap Q_1 = \emptyset$ **or** $\mathcal{P}\cap Q_3 = \emptyset$ **then**
9: `ISSguaranteed` $\leftarrow$ **true**
10: **else**
11: Calculate $\phi_{\max}$ and $\phi_{\min}$ as in (19) and (20), respectively
12: **if** $\phi_{\max} < \phi_{\min} + \pi$ **then**
13: `ISSguaranteed` $\leftarrow$ **true**
14: **end if**
15: **end if**
16: **end if**
17: $k \leftarrow k + \Delta k$
18: **end while**
19: **end if**
20: **return** `ISSguaranteed`

3.2. Optimization problem solution strategy

The procedure for verifying the conditions of Theorem 1 in Algorithm 1, to verify whether the closed-loop system is ISS for given parameters θ, allows devising a data-driven approach for solving the settling time optimization problem (12). To this end, inspired by the approach in Weekers et al. (2025), we break down the optimization problem into a cascade of two optimization problems with continuous cost functions to circumvent the extreme sensitivity of the settling time

$t_s(\theta)$ to changes in the parameters θ. In this cascaded optimization approach, the inner optimization loop is aimed at solving

$$\theta^*(\tau) := \arg\min_{\theta\in\Theta} J(\tau,\theta) \tag{23a}$$

$$\text{s.t.} \max_{t\in[t_r+\tau,T]} |e(t,\theta)| \le e_b, \tag{23b}$$

where $J(\tau,\theta)$ is a cost function continuous in θ for any fixed value of τ, that will be defined shortly. The outer optimization loop is aimed at minimizing the settling time by minimizing τ subject to the constraint that the problem in (23) is feasible, i.e., subject to the constraint that there indeed exist parameters θ such that the error $e(t,\theta)$ satisfies the desired error bound e_b for all $t \in [t_r+\tau, T]$. That is, the outer optimization loop is aimed at solving

$$\tau^* := \arg\min_{\tau\in[0,T-t_r]} \tau \tag{24a}$$

$$\text{s.t. (23) has a feasible solution.} \tag{24b}$$

Note that solving the reformulated problem (23)–(24) is equivalent to solving the original settling time optimization problem (11)–(12), as given by the following proposition.

Proposition 1. *For the original problem (11)–(12), and the reformulated problem (23)–(24), it holds that* $\tau^* = t_s^*$.

Proof. By definition of t_s^* in (11)–(12), there exists a $\theta' \in \Theta$ such that $\max_{t\in[t_r+t_s^*,T]} |e(t,\theta')| \le e_b$. Hence, (23) is feasible for $\tau = t_s^*$, and thus $\tau^* \le t_s^*$ by (24). Moreover, by definition of t_s^* in (11)–(12) it follows that $\max_{t\in[t_r+\tau,T]} |e(t,\theta)| > e_b$ for any $\theta \in \Theta$ if $\tau < t_s^*$. Therefore, (23) is not feasible for any $\tau < t_s^*$, showing that $\tau^* \ge t_s^*$. Since it holds both that $\tau^* \le t_s^*$ and that $\tau^* \ge t_s^*$, it follows that $\tau^* = t_s^*$, which completes the proof. □

Since the cost functions in (23a) and (24a) are continuous in their respective optimization variables, the extreme sensitivity of the optimization variables to the cost function is mitigated by solving the reformulated problem (23)–(24) instead of the original problem (11)–(12). Moreover, note that the reformulated problem is independent of the chosen cost function $J(\tau,\theta)$. This cost function therefore mainly serves to guide the search direction for a feasible solution, and to indicate which parameters θ to favor in case finding the exact solution to the optimization problem might not be possible (common in practice, where optimization problems are typically only solved to a desired tolerance). To exploit the overshoot-reducing capabilities of the HIGS (Van den Eijnden, Heertjes, Heemels et al., 2020; Van Dinther et al., 2021), we define $J(\tau,\theta)$ as

$$J(\tau,\theta) := \int_{t_r}^{t_r+\tau} |e(t,\theta)|\,\mathrm{d}t, \tag{25}$$

i.e., as the absolute integral error over a time interval of duration τ after the reference motion has finished. This cost function penalizes overshoot, and thus steers the optimization algorithm more quickly towards solutions with lower overshoot, which is often beneficial for faster settling times.

The main challenge in solving the reformulated problem in (23)–(24) is in verifying satisfaction of the constraint (24b). This challenge results from the fact that it is a priori unknown for a given value of τ if, and for which $\theta \in \Theta$, it holds that $t_s(\theta) \le \tau$, i.e., that the constraint (23b) is satisfied. Furthermore, the inner optimization (23) is not necessarily convex. Therefore, to assess the feasibility of (23), we choose to use (a modified version of) the DIRECT algorithm (Jones & Martins, 2021; Jones et al., 1993) as it is a global optimization algorithm that is well-suited for optimizing non-convex and non-smooth cost functions. This optimization algorithm repeatedly samples points from the search space $\Omega := \{\theta = [\theta_1,\dots,\theta_{n_\theta}] : \theta_i \in [\underline{\theta}_i, \bar{\theta}_i]^\intercal, i = 1,\dots,n_\theta\}$, where $\underline{\theta}_i$ and $\bar{\theta}_i$, $i = 1,\dots,n_\theta$, denote, respectively, lower and upper bounds on the elements θ_i of θ, and divides it into progressively smaller hyperrectangles to balance between local and global search, in an attempt to solve the optimization problem in (23) (for visualizations of the algorithm the reader is referred to Jones et al. (1993) and Jones and Martins (2021)). In doing so, the points sampled by the DIRECT algorithm form a dense subset of Ω as the number of iterations approaches infinity (see, e.g., Jones et al. (1993)), meaning that for any $\theta \in \Omega$, and any $\delta > 0$, a point within a distance δ from θ will be sampled eventually. Under the assumption that for a given value of τ, if (23) is feasible, there exist a point $\theta' \in \Theta$ and a $\delta > 0$ such that (23) is feasible for any θ within a distance δ from θ', such feasible point will thus be found with a sufficiently large number of iterations. Hence, if no feasible solution is found to (23) after a sufficiently large number of iterations, it can be concluded that (23) is not feasible.

The modified version of the DIRECT algorithm used to solve the inner optimization problem, which is given in Algorithm 2, is largely aligned with the modified version of the algorithm used in Weekers et al. (2025). However, the following two modifications to the version of Weekers et al. (2025) can be recognized in Algorithm 2:

(i) While the constraint handling approach for the feasibility constraint $\theta \in \Theta$ is the same as in Weekers et al. (2025) (i.e., assigning a surrogate cost value $\widetilde{J}$ determined using the strategy in Gablonsky (2001, Sec. 3.4.3) instead of performing a measurement when the constraint is not satisfied), the method for verifying the condition in lines 2 and 17 are different: instead of drawing the Nyquist contour and evaluating the maximum value of the sensitivity function to verify whether the closed-loop system is asymptotically stable with sufficient robustness margin to plant uncertainties, here we use Algorithm 1 to verify whether the closed-loop system is guaranteed to be ISS for the to-be-evaluated parameters θ, to ensure that measurements are only performed with parameters for which the closed-loop system is guaranteed to be ISS.

(ii) In Weekers et al. (2025), a stopping condition of the form $J^*(\tau) \le e_b$ with $J^*(\tau) := J(\tau,\theta^*)$ the optimal cost for the inner optimization problem (23), is used to prevent unnecessary function evaluations in case the constraint (24b) is already known to be satisfied (and thus τ can be decreased in the bisection search from Algorithm 3 below). Since we use a different cost function (25) than in Weekers et al. (2025), we cannot use the same condition to evaluate whether the constraint (24b) is satisfied. Therefore, instead, we use a different stopping condition of the form $\max_{t\in[t_r+\tau,T]}|e(t,\theta)| \le e_b$ in lines 4–7 and lines 19–22 in Algorithm 2 below (we have highlighted modifications (i) and (ii) in gray).

Algorithm 2: Modified DIRECT algorithm for solving the inner optimization problem (23), (25). Modifications with respect to Weekers et al. (2025) are highlighted in gray.

Input: lower bounds $\underline{\theta}_i$ and upper bounds $\bar{\theta}_i$, $i = 1,2,\dots,n_\theta$, on the parameters $\theta = [\theta_1 \ \cdots \ \theta_{n_\theta}]^\intercal$, cost function (25), function evaluation budget N, iteration budget M, parameter $\varepsilon > 0$ indicating the desired relative accuracy of the solution (e.g., 10^{-4}) (Jones & Martins, 2021), error bound e_b, current value of τ, and lookup table $\mathcal{E}$ containing previous inputs θ and corresponding outputs $e(t,\theta)$ obtained during previous iterations of solving the problem in (23), (25), or initialized as an empty list if not available.

Output: found optimal parameters $\theta^*(\tau)$ and updated lookup table $\mathcal{E}$.

1: Take θ_1 to be the center of the search space $\Omega := \{\theta = [\theta_1,\dots,\theta_{n_\theta}]^\intercal : \theta_i \in [\underline{\theta}_i, \bar{\theta}_i], i = 1,2,\dots,n_\theta\}$.
2: **if** ISSguaranteed for θ_1 **then** // Algorithm 1
3: Evaluate (25) by obtaining $e(t,\theta_1)$ from the lookup table

$\mathcal{E}$ if $\theta_1 \in \mathcal{E}$, or from a measurement if $\theta_1 \notin \mathcal{E}$: $J_1 \leftarrow J(\tau, \theta_1)$. Add θ_1 and $e(t, \theta_1)$ to $\mathcal{E}$ if $\theta_1 \notin \mathcal{E}$.
4: **if** $\max_{t\in[t_r+\tau,T]} |e(t,\theta_1)| \le e_b$ **then**
5: Save the current best cost $J^* \leftarrow J_1$ and corresponding parameters $\theta^*(\tau) \leftarrow \theta_1$.
6: Jump to line 31.
7: **end if**
8: **else**
9: Assign a surrogate cost value according to the strategy in (Gablonsky, 2001, Sec. 3.4.3): $J_1 \leftarrow \widetilde{J}$.
10: **end if**
11: Initialize the function evaluation and iteration counters $n \leftarrow 1$, $m \leftarrow 0$, and save the current best cost $J^* \leftarrow J_1$.
12: **while** $n < N$ **and** $m < M$ **do**
13: Identify the set S of all indices $s \in \{1, 2, \dots, n\}$ for which there exists a $K > 0$ such that, $\forall j \in \{1, 2, \dots, n\}$,

$$J_s - Kd_s \le \min\{J^* - \varepsilon|J^*|, J_j - Kd_j\},$$

where d_j is the longest side length of hyperrectangle j.
14: **for all** $s \in S$ **do**
15: **for** $k = 1$ **to** 2 **do**
16: Take $\widetilde{\theta}_k \leftarrow \theta_s + \frac{1}{3}(-1)^k d_s \boldsymbol{\sigma}$ to be the new to-be-evaluated point, where θ_s denotes the center of hyperrectangle s, and $\boldsymbol{\sigma}$ the unit vector in the direction along which the hyperrectangle has length d_s. If the hyperrectangle s has multiple sides of length d_s, choose the direction with the smallest number of total subdivisions.
17: **if** ISSguaranteed for $\widetilde{\theta}_k$ **then** // Algorithm 1
18: Evaluate (25) by obtaining $e(t, \widetilde{\theta}_k)$ from the lookup table $\mathcal{E}$ if $\widetilde{\theta}_k \in \mathcal{E}$, or from a measurement if $\widetilde{\theta}_k \notin \mathcal{E}$: $J_{n+k} \leftarrow J(\tau, \widetilde{\theta}_k)$. Add $\widetilde{\theta}_k$ and $e(t, \widetilde{\theta}_k)$ to $\mathcal{E}$ if $\widetilde{\theta}_k \notin \mathcal{E}$.
19: **if** $\max_{t\in[t_r+\tau,T]} |e(t,\widetilde{\theta}_k)| \le e_b$ **then**
20: Save the current best cost $J^* \leftarrow J_{n+k}$ and corresponding parameters $\theta^*(\tau) \leftarrow \widetilde{\theta}_k$.
21: Jump to line 31.
22: **end if**
23: **else**
24: Assign a surrogate cost value according to the strategy in (Gablonsky, 2001, Sec. 3.4.3): $J_{n+k} \leftarrow \widetilde{J}$.
25: **end if**
26: **end for**
27: Increment function evaluation counter $n \leftarrow n + 2$, and trisect hyperrectangle s along the direction $\boldsymbol{\sigma}$.
28: **end for**
29: Increment iteration counter $m \leftarrow m+1$, and save the current best cost $J^* \leftarrow \min\{J_j : j = 1, 2, \dots, n\}$ and corresponding parameters θ^*. In case multiple evaluations resulted in the same cost J^*, take the parameters corresponding to the evaluation with the lowest index.
30: **end while**
31: **return** parameters $\theta^*(\tau)$ and the updated lookup table $\mathcal{E}$.

Besides this modified DIRECT algorithm to solve the feasibility problem, we adopt a bisection search to solve the outer optimization problem (24) up to a desired precision $\Delta\tau$, similar to Weekers et al. (2025). In this bisection search, the inner optimization problem (23), (25) is solved at each iteration of the search to evaluate the constraint (24b), as illustrated in Algorithm 3.

Algorithm 3: Bisection search for solving the outer optimization problem (24).

Input: initial lower bound $\underline{\tau}$ and upper bound $\bar{\tau}$ on τ, desired precision $\Delta\tau$, and error bound e_b.

Output: found optimal value τ^* and corresponding parameters $\theta^*(\tau^*)$.

1: **while** $|\bar{\tau} - \underline{\tau}| > \Delta\tau$ **do**
2: $\tau \leftarrow (\bar{\tau} + \underline{\tau})/2$.
3: Evaluate satisfaction of the constraint (24b) by solving the problem in (23), (25). // Algorithm 2.
4: **if** (24b) is satisfied **then**
5: $\bar{\tau} \leftarrow \tau$.
6: **else**
7: $\underline{\tau} \leftarrow \tau$.
8: **end if**
9: **end while**
10: $\tau^* \leftarrow \bar{\tau}$.
11: **return** found optimal value τ^* and corresponding parameters $\theta^*(\tau^*)$.

The interconnection of the (modified) DIRECT algorithm with the closed-loop system Σ forms a sampled-data extremum-seeking control (ESC) loop in the spirit of Khong, Nešić, Manzie et al. (2013), Khong, Nešić, Tan et al. (2013). Hence, the addition of the bisection search results in a cascaded ESC loop.

4. Industrial case study

In this section, we perform an industrial case study of the proposed cascaded ESC approach for HIGS-based controller tuning on a wire bonder system. First, in Section 4.1, we describe the use case and define the controller structure. Then, in Section 4.2, we apply the proposed approach to an industrial wire bonding machine.[1]

4.1. Wire bonder system

Wire bonders are systems used in the manufacturing process of semiconductors to create wired interconnections between integrated circuits and their packaging. These interconnections are made by performing rapid point-to-point movements along the wire bonder's x-, y-, and z-motion axes illustrated in Fig. 8. To ensure satisfactory quality of the finished product, the positioning error of the wire bonder should not exceed an error bound e_b at the moment that the wired connection is made. This error bound is typically in the micrometer range, so that the wires are positioned correctly and do not touch each other. Furthermore, the high throughput demands of placing in the order of ten wires per second require this accuracy to be reached as quickly as possible. Hence, as is the case in many industrial use cases, the goal is to minimize the settling time $t_s(\theta)$ in order to increase throughput. In particular, we take the dynamics of the wire bonder along the x-axis as our plant P.

Remark 2. By considering only a single motion axis, the plant P forms a single-input-single-output (SISO) system. This choice is motivated by the fact that in practice the wire bonder motion axes are sufficiently decoupled to consider them as SISO systems. The main challenge in extending our framework to multi-input-multi-output (MIMO) systems is in guaranteeing input-to-state stability of the closed-loop system, since the stability conditions of Theorem 1 and consequently the procedure in Algorithm 1 are only valid for SISO systems. An extension towards MIMO systems, e.g., using the frequency-domain conditions presented in Beerens et al. (2024), could therefore be an interesting research direction for future work.

The motion axes of a wire bonder are typically controlled using linear PID control, combined with low-pass filtering and notch filters. However, given the potential performance benefits of using HIGS-based

[1] Some results in this section are normalized for confidentiality reasons.

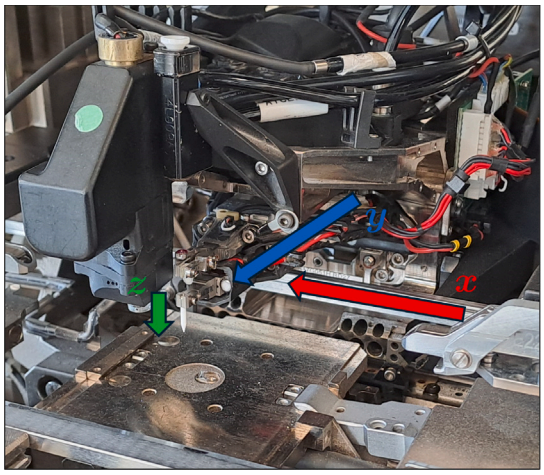

Fig. 8. The wire bonder motion stage consisting of an x-motion axis, a y-motion axis, and a z-motion axis stacked on top of each other.

controllers, here we replace this linear controller by a HIGS-based counterpart. For ease of exposition, we omit the notch filters and use only a first-order low-pass filter in addition to the PID components. The used HIGS-based controller is constructed by a linear lead–lag filter

$$C_{ll}(s) = k_p \frac{\omega_{p_{ll}}(s+\omega_{z_{ll}})}{\omega_{z_{ll}}(s+\omega_{p_{ll}})} \tag{26}$$

with gain k_p, lead frequency $\omega_{z_{ll}}$, and lag frequency $\omega_{p_{ll}}$, and a HIGS-based integrator $C_i\{\mathcal{H}\}$ as illustrated in Fig. 4, with $H(s)$ as in (4) and $C^*(s) = C_i(s) = \omega_i/s$. The frequency-lifting filter W is chosen to be a proper filter that acts as a second-order low-pass filter to minimize high-frequency switching of the HIGS and is chosen as

$$W(s) = \frac{\omega_p^2(s+\omega_z)^2}{\omega_z^2(s+\omega_p)^2} \tag{27}$$

with zeros ω_z and poles ω_p. The resulting[2] closed-loop system with HIGS-based controller $C\{\mathcal{H}\}$ is illustrated in Fig. 9, and has eight tunable parameters, namely: the parameters k_p, $\omega_{z_{ll}}$, and $\omega_{p_{ll}}$ of the lead–lag filter C_{ll}, the HIGS parameters k_h and ω_h, the integrator frequency ω_i of C_i, and the zeros ω_z and the poles ω_p of the frequency-lifting filter W. However, due to the factor $1/k_h$ in the pre-filter H^{-1} (cf. (4)), k_h only affects the combination of H^{-1} and the HIGS $\mathcal{H}$ in the ratio ω_h/k_h determining the corner frequency of the HIGS. Hence, we can choose $k_h = 1$ without loss of generality. Furthermore, the zeros ω_z of the frequency-lifting filter W mainly serve to make W bi-proper, and can thus remain fixed and chosen sufficiently large to not influence the desired low-pass characteristics of W. In our case we have chosen $\omega_z = \pi f_s/4$, with f_s the sample frequency in Hertz (typically in the order of several kilohertz) as decreasing ω_z results in reduced error suppression while increasing ω_z gives no further benefits. With these observations, the remaining six parameters $\boldsymbol{\theta} := [k_p\ \omega_{z_{ll}}\ \omega_{p_{ll}}\ \omega_h\ \omega_i\ \omega_p]^\intercal$ serve as the parameters to be tuned by the proposed cascaded ESC algorithm.

To evaluate the efficacy of the proposed ESC framework in minimizing the settling time, we compare the settling performance of a HIGS-based controller tuned using the proposed ESC framework to both a HIGS-based controller and a linear controller in which the parallel path containing the HIGS in Fig. 9 is replaced by a linear integrator, which are tuned using a proprietary state-of-the-art frequency-based auto-tuner (FBA) used in industry. This FBA tunes controllers based on (measured) FRF data of the plant P, by using particle swarm optimization to maximize the bandwidth given a user-defined frequency-dependent upper bound on the sensitivity function. Since such a sensitivity function is not available for HIGS-based controllers, due to the nonlinear nature of the HIGS, an approximation based on the describing function of the HIGS in (3) is used instead. We care to stress that by using such an approximation without additional stability checks such as Algorithm 1, the FBA is unable to guarantee that the closed-loop system is ISS for the resulting controller (see also the discussion at the end of Section 2.1). Moreover, due to the reliance on the describing-function-based approximation in the FBA, the parameters ω_z and ω_p of the frequency-lifting filter W cannot be tuned using the FBA, as the influence of W is not visible in the describing-function-based approximation of the frequency domain characteristics (cf. Section 2.2). Therefore, we omit the frequency-lifting filter W for the controllers tuned by the FBA. It is important to keep these differences in structure, tuning possibilities, and potential robustness in mind when comparing the respective controllers.

4.2. Experimental validation

Next, we compare the performance of the three different controllers. We will refer to the controller tuned using our ESC framework as the ESC HIGS controller, and to the HIGS-based and linear controllers tuned using the FBA, respectively, as the FBA HIGS and FBA linear controllers. We set all lower bounds on the controller parameters to zero for the ESC HIGS controller, and use the values shown in Table 1 as upper bounds. These upper bounds are based on engineering insights obtained by results from the FBA, and a trade-off between sufficient room for optimization and the available amount of function evaluations. Note that the upper bounds on ω_h and ω_i are both chosen lower than the parameters of the FBA HIGS controller; the reason for this is the observation that such higher values in general did not pass the stability check of Algorithm 1 and are therefore excluded to reduce the size of the search space Ω. We choose the increment $\Delta k = 1$ until $k = 50$, and $\Delta k = 10$ thereafter until $k = \bar{k} = 500$ in Algorithm 1. Furthermore, we use an upper bound of 8 dB on the (describing function-based approximation of the) sensitivity function for frequencies up to $0.05625 f_s$ (around the first resonance) and 2.5 dB thereafter in the FBA, and opt to include the same constraint on the describing-function-based approximation of the sensitivity function in our framework to allow a fairer comparison. This constraint is handled in the same way as the sensitivity constraint in Weekers et al. (2025). The reference motion consists of a cycloidal (Biagiotti & Melchiorri, 2008, Sec. 2.2.2) forward and backward movement of four millimeters along the x-axis, and the constraint (24b) is only said to be satisfied for a given value of τ in case it is satisfied for both motion directions. By only considering the constraint (24b) to be satisfied for a given value of τ if it is satisfied for both motion directions, we essentially aim to minimize the worst-case settling time over both motion directions. The initial lower bound $\underline{\tau}$ and upper bound $\bar{\tau}$ on τ for the bisection search are chosen as $80/f_s$ and $240/f_s$, respectively, for the ESC HIGS controller based on insights of settling time of the FBA HIGS controller.

We choose the function evaluation budget N and the iteration budget M both equal to 10 000. Furthermore, we choose the desired precision of the bisection search equal to ten samples, i.e., $\Delta\tau = 10/f_s$, resulting in four iterations of the bisection search to be performed. During these four iterations, in total 34 698 function evaluations were performed. Of these function evaluations, only 960 resulted in real motion experiments, due to the use of the lookup table $\mathcal{E}$ and motion experiments only being performed if the closed-loop system is guaranteed to be ISS. With the duration of the motion experiments being in the order of hundreds of milliseconds, the total optimization time was thus in the order of ten minutes.

[2] The actual implementation on the system is done using Tustin discretization of the continuous-time filters presented in this section.

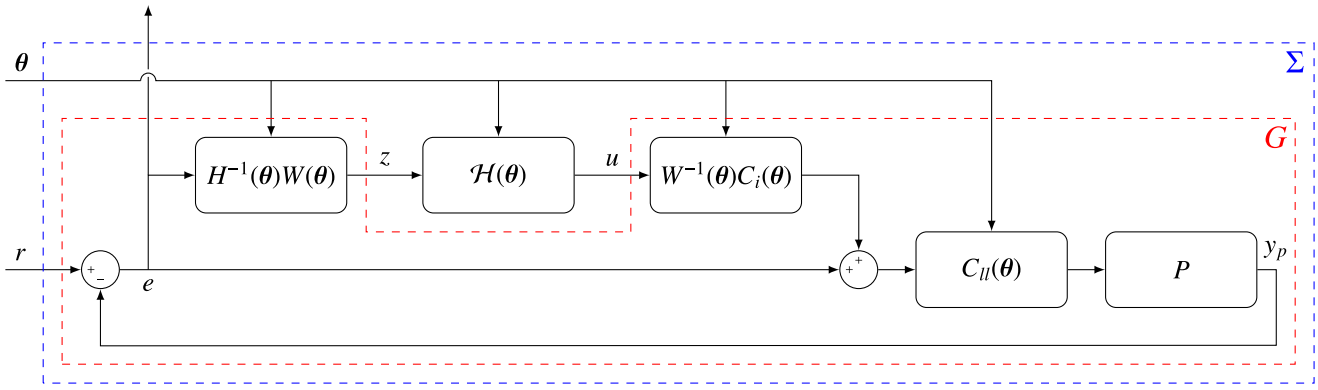

Fig. 9. Block scheme illustrating the generalized plant G, consisting of the plant P, and lead–lag controller C_{ll}, integrator C_i, frequency-lifting filter W, and magnitude filter H parametrized by tunable parameters θ. The feedback interconnection of G and a HIGS $\mathcal{H}(\theta)$ parametrized by θ forms a multi-input-single-output system Σ with inputs r and θ, and output e.

Table 1
Parameter upper bounds and values for each controller for the experimental case study.

	Bound	ESC HIGS	FBA HIGS	FBA linear
k_p	0.715	0.34573	0.44286	0.60369
$\omega_{z_{ll}}$	$0.015\pi f_s$	$0.00639\pi f_s$	$0.01205\pi f_s$	$0.01351\pi f_s$
$\omega_{p_{ll}}$	$0.13125\pi f_s$	$0.05590\pi f_s$	$0.07542\pi f_s$	$0.07343\pi f_s$
ω_h	$0.01\pi f_s$	$0.00438\pi f_s$	$0.01036\pi f_s$	N/A
ω_i	$0.01\pi f_s$	$0.00907\pi f_s$	$0.01024\pi f_s$	$0.00595\pi f_s$
ω_p	$0.25\pi f_s$	$0.01389\pi f_s$	N/A	N/A

Table 2
Settling times $t_s(\theta)$ (worst-case over 5 repetitions) for each controller and motion direction.

	Forward movement	Backward movement
ESC HIGS	$168/f_s$	$205/f_s$
FBA HIGS	$146/f_s$	$260/f_s$
FBA linear	$142/f_s$	$260/f_s$

The resulting parameters of all three controllers are given in Table 1. With these parameters, the ESC HIGS controller results in a significantly faster worst-case settling time (considering five validation runs for each respective controller in both motion directions) than both the FBA HIGS and the FBA linear controller ($205/f_s$ instead of $260/f_s$, i.e., a reduction of more than 21%), as illustrated by the dashed colored vertical lines in Fig. 10 and the values in Table 2. This reduction in worst-case settling time is mainly the result of the error response for the ESC HIGS controller satisfying the error bound around $t = 410/f_s$ during the backward motion, while the responses for the FBA HIGS and the FBA linear controllers violate the error bound around this time instance. However, while the response for the ESC HIGS controller satisfies the error bound around this time instance, it is close to this bound. This can be seen from the jump in the settling time from around $205/f_s$ to around $251/f_s$ that occurs for the ESC HIGS controller when decreasing the error bound to below $0.98e_b$, as shown in Fig. 11. This jump in settling time illustrates its discontinuous nature discussed before. Nevertheless, despite this jump in settling time, the worst-case settling time for the ESC HIGS controller remains still around 3.5% lower than the worst-case settling time for the FBA controllers in this case. In fact, the backward motion is the limiting factor for the worst-case settling time for the whole error bound range shown in Fig. 11, and the ESC HIGS controller has the lowest settling time for nearly the whole range. In addition, the ESC HIGS controller has the additional benefit that the closed-loop system is guaranteed to be ISS based on Theorem 1; something which is not the case for the FBA HIGS controller. Despite the fact that the FBA HIGS controller

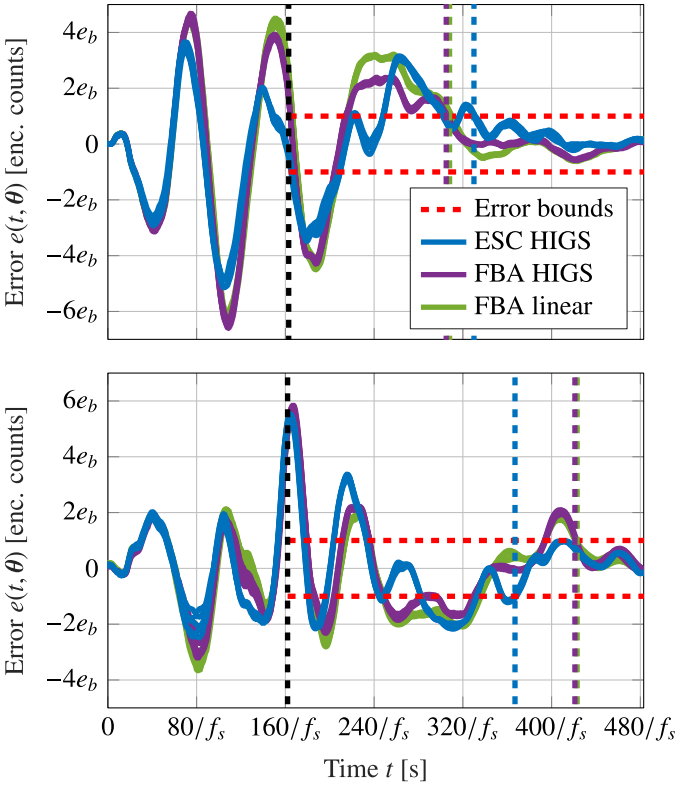

Fig. 10. Real servo error $e(t,\theta)$ obtained for the three controllers during five repetitions of the forward (top) and backward (bottom) motion. The worst-case settling time for the ESC HIGS controller (considering all repetitions in both motion directions) is significantly (21%) shorter, as illustrated by the distance between the dashed black vertical line indicating the end of the motion (t_r), and the dashed colored vertical lines indicating the time instances where the error last violates the error bound e_b. (For interpretation of the references to color in this figure legend, the reader is referred to the web version of this article.)

seems to result in stable system behavior, as illustrated by the response shown in Fig. 10, it does not pass the test in Algorithm 1 to guarantee that the closed-loop system with this controller is ISS. A potential direction for future research could therefore be to investigate whether (i) this illustrates conservatism in Algorithm 1 for the satisfaction of the conditions of Theorem 1, (ii) this illustrates conservatism in the conditions of Theorem 1 for guaranteeing input-to-state stability, or (iii)

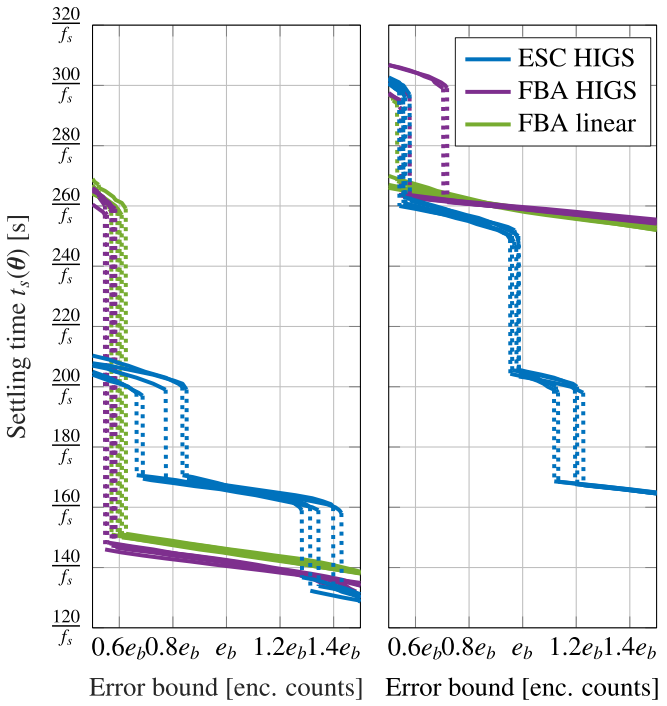

Fig. 11. Settling times obtained with different error bounds e_b for the three controllers during five repetitions of the forward (left) and backward (right) motion. The large jumps in settling time clearly illustrate the discontinuous nature of the metric.

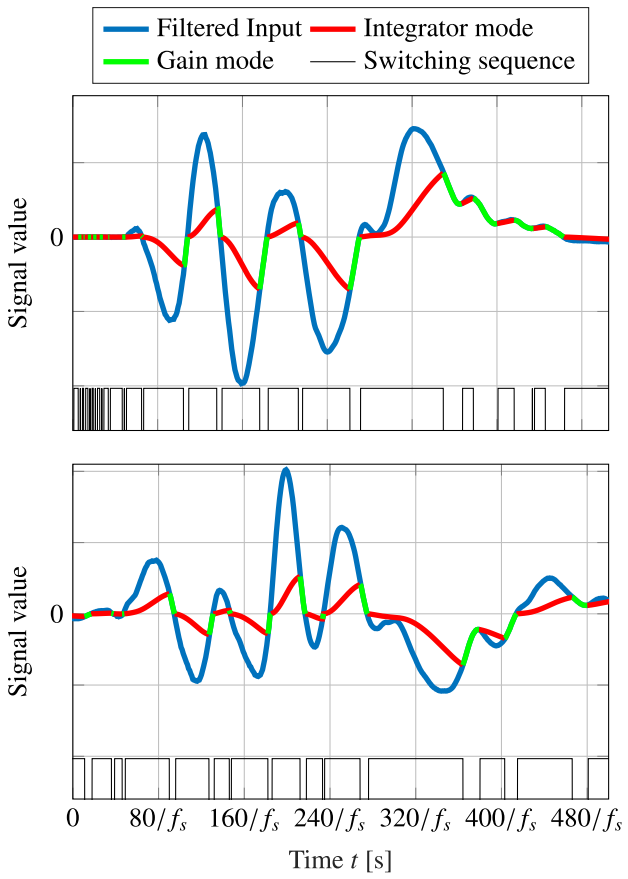

Fig. 12. HIGS input/output of the forward motion (top) and backward motion (bottom) with gain-mode illustrated in green and integrator mode illustrated in red. The switching points between the two modes are indicated at the bottom in black. (For interpretation of the references to color in this figure legend, the reader is referred to the web version of this article.)

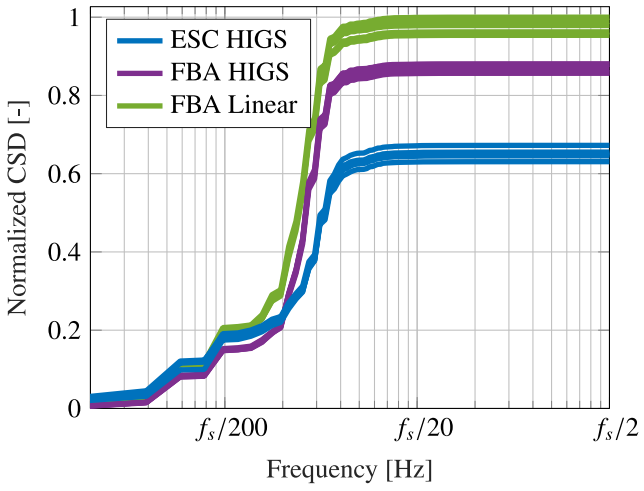

Fig. 13. Cumulative energy spectral density of the error of the five motions of the different controllers, with the FBA-tuned HIGS-based controller (FBA HIGS), FBA-tuned linear controller (FBA linear) and the ESC-tuned HIGS-based controller (ESC HIGS).

the closed-loop system is not ISS for the HIGS-based controller tuned by the FBA.

It is important to note that in the case where a linear integrator would give better results, the ESC tuning algorithm would be able to choose ω_h large to ensure the response of the HIGS-based integrator approaches that of a linear integrator, since in this case the HIGS will remain in gain mode with gain $k_h = 1$. We can evaluate if this is the case for the ESC HIGS controller by looking at the switching characteristics of the HIGS shown in Fig. 12. The HIGS output is divided into the two responses: the gain-mode response is illustrated in green and the integrator mode in red. From Fig. 12, it becomes apparent that ω_h is chosen sufficiently small such that the HIGS is indeed switching between the integrator mode and the gain mode. The input of the HIGS in Fig. 12 also indicates that, despite the use of the lead filter H^{-1} that amplifies high-frequency signals before the HIGS, the HIGS input is a clean signal without high-frequency contributions with large amplitudes, illustrating the success of the proposed pre- and post-filtering technique of Section 2.2.

An alternative analysis of the performance of the controllers besides the settling time performance measure is often done using the cumulative energy spectral density (CSD) of the tracking error, as it is directly correlated to the cumulative root-mean-square of the error and therefore provides a good indication of the overall disturbance rejection capabilities of the controllers. From the CSD for the three controllers, it can be concluded that the HIGS-based controllers have more disturbance rejection compared to the linear controller, as shown in Fig. 13. Furthermore, Fig. 13 shows that the ESC-tuned HIGS-based controller results in a lower CSD compared to the FBA-tuned HIGS-based controller. This reduction in CSD indicates that the proposed data-driven time-domain tuning approach in this case not only improves settling time performance, but also improves disturbance rejection capabilities.

5. Conclusions

In this work, we developed a data-driven approach based on sampled-data extremum-seeking control for tuning of controllers based on so-called hybrid integrator-gain systems. In particular, the proposed approach is aimed at optimizing the settling time in point-to-point tasks. This work was motivated by (i) the potential performance benefits of nonlinear and/or hybrid controllers for the performance of

linear (motion) systems, (ii) the lack of industrial adoption of nonlinear and/or hybrid controllers due to their increased design complexity, and (iii) the time-consuming nature of (nonlinear) controller design (especially, e.g., in the presence of machine-to-machine variations). To facilitate the data-driven tuning approach, we in addition developed an automated procedure for guaranteeing that the closed-loop system is ISS throughout and after the tuning process, based solely on non-parametric (measured) frequency-response function data of the plant. The proposed approach is tested with a case study on an industrial wire bonder system, in which the framework is able to tune a HIGS-based controller that results in stable responses with improved settling times when compared to tuning methods currently used in industry. Future work could consider application to higher-order controllers or other nonlinear techniques, e.g., variable-gain control.

CRediT authorship contribution statement

Jonas G. Hendrikx: Writing – original draft, Visualization, Validation, Software, Methodology, Investigation, Formal analysis. **Wouter Weekers:** Writing – review & editing, Writing – original draft, Software, Methodology, Conceptualization. **Luke F. van Eijk:** Writing – review & editing, Validation, Resources, Methodology, Conceptualization. **Marcel F. Heertjes:** Writing – review & editing, Supervision. **Nathan van de Wouw:** Writing – review & editing, Supervision, Project administration, Funding acquisition, Conceptualization.

Declaration of competing interest

The authors declare that they have no known competing financial interests or personal relationships that could have appeared to influence the work reported in this paper.

Acknowledgments

The authors would like to thank Dragan Kostić for his valuable feedback during the execution of this work, and Niels van der Venne and Kai Wa (Kelvin) Yan for their help in preparing the wire bonder system for the experiments.

This publication is part of the project Digital Twin with project number P18-03 of the research program TTW Perspective which is (partly) financed by the Dutch Research Council (NWO), Netherlands.

References

Abidi, K., & Sabanovic, A. (2007). Sliding-mode control for high-precision motion of a piezostage. *IEEE Transactions on Industrial Electronics*, *54*(1), 629–637.

Ahn, H.-S., Chen, Y., & Moore, K. L. (2007). Iterative learning control: Brief survey and categorization. *IEEE Transactions on Systems, Man, and Cybernetics, Part C (Applications and Reviews)*, *37*(6), 1099–1121.

Ariyur, K. B., & Krstic, M. (2003). *Real-time optimization by extremum-seeking control*. John Wiley & Sons.

Beerens, R., Konings, P., Heertjes, M., & Van den Eijnden, S. (2024). Stability and performance assessment of a MIMO HIGS-based controller design. In *2024 European control conference* (pp. 1723–1728). IEEE.

Beker, O., Hollot, C. V., & Chait, Y. (2001). Plant with integrator: an example of reset control overcoming limitations of linear feedback. *IEEE Transactions on Automatic Control*, *46*(11), 1797–1799.

Biagiotti, L., & Melchiorri, C. (2008). *Trajectory planning for automatic machines and robots*. Springer Berlin Heidelberg.

Chen, J. (1995). Sensitivity integral relations and design trade-offs in linear multivariable feedback systems. *IEEE Transactions on Automatic Control*, *40*(10), 1700–1716.

Chu, H., van Den Eijnden, S., Heertjes, M., & Heemels, W. (2024). Filtering in projection-based integrators for improved phase characteristics. In *2024 IEEE 63rd conference on decision and control* (pp. 2391–2396). IEEE.

Clegg, J. C. (1958). A nonlinear integrator for servomechanisms. *Transactions of the American Institute of Electrical Engineers, Part II: Applications and Industry*, *77*(1), 41–42.

Deenen, D. A., Heertjes, M. F., Heemels, W. P. M. H., & Nijmeijer, H. (2017). Hybrid integrator design for enhanced tracking in motion control. In *2017 American control conference* (pp. 2863–2868).

Franklin, G. F., Powell, J. D., & Emami-Naeinim, A. (2015). *Feedback control of dynamic systems, global edition* (7th ed.). Pearson.

Freudenberg, J., Middleton, R., & Stefanpoulou, A. (2000). A survey of inherent design limitations. *vol. 5*, In *Proceedings of the 2000 American control conference* (pp. 2987–3001).

Gablonsky, J. M. X. (2001). *Modifications of the DIRECT algorithm* (Ph.D. thesis), North Carolina State University.

Grassi, E., Tsakalis, K. S., Dash, S., Gaikwad, S. V., MacArthur, W., & Stein, G. (2001). Integrated system identification and PID controller tuning by frequency loop-shaping. *IEEE Transactions on Control Systems Technology*, *9*(2), 285–294.

Heertjes, M. F., Hoogeveen, T. P., & Eijnden, S. J. v. d. (2024). Stage motion control: Nonlinear integrators revisited. *Annual Review of Control, Robotics, and Autonomous Systems*, *8*.

Heertjes, M., Irigoyen Perdiguero, N., & Deenen, D. (2019). Robust control and data-driven tuning of a hybrid integrator-gain system with applications to wafer scanners. *International Journal of Adaptive Control and Signal Processing*, *33*(2), 371–387.

Heertjes, M. F., Schuurbiers, X. G. P., & Nijmeijer, H. (2009). Performance-improved design of N-PID controlled motion systems with applications to wafer stages. *IEEE Transactions on Industrial Electronics*, *56*(5), 1347–1355.

Heertjes, M. F., Van den Eijnden, S. J. A. M., Heemels, W. P. M. H., & Nijmeijer, H. (2021). A solution to gain loss in hybrid integrator-gain systems. In *2021 IEEE conference on control technology and applications* (pp. 1179–1184).

Hjalmarsson, H., Gevers, M., Gunnarsson, S., & Lequin, O. (1998). Iterative feedback tuning: theory and applications. *IEEE Control Systems Magazine*, *18*(4), 26–41.

Hunnekens, B. G. B., Van de Wouw, N., & Nešić, D. (2016). Overcoming a fundamental time-domain performance limitation by nonlinear control. *Automatica*, *67*, 277–281.

Jones, D. R., & Martins, J. R. R. A. (2021). The DIRECT algorithm: 25 years later. *Journal of Global Optimization*, *79*(3), 521–566.

Jones, D. R., Perttunen, C. D., & Stuckman, B. E. (1993). Lipschitzian optimization without the Lipschitz constant. *Journal of Optimization Theory and Applications*, *79*, 157–181.

Khong, S. Z., Nešić, D., Manzie, C., & Tan, Y. (2013). Multidimensional global extremum seeking via the DIRECT optimisation algorithm. *Automatica*, *49*(7), 1970–1978.

Khong, S. Z., Nešić, D., Tan, Y., & Manzie, C. (2013). Unified frameworks for sampled-data extremum seeking control: Global optimisation and multi-unit systems. *Automatica*, *49*(9), 2720–2733.

Skogestad, S., & Postlethwaite, I. (2005). *Multivariable feedback control: analysis and design*. John Wiley & Sons.

Sontag, E. D., & Wang, Y. (1995). On characterizations of the input-to-state stability property. *Systems & Control Letters*, *24*(5), 351–359.

Van de Wouw, N., Pastink, H. A., Heertjes, M. F., Pavlov, A. V., & Nijmeijer, H. (2008). Performance of convergence-based variable-gain control of optical storage drives. *Automatica*, *44*(1), 15–27.

Van den Eijnden, S. J. A. M. (2022). *Hybrid integrator-gain systems: Analysis, design, and applications* (Ph.D. thesis), Eindhoven University of Technology, ISBN: 978-90-386-5506-2.

Van den Eijnden, S. J. A. M., Heertjes, M. F., Heemels, W. P. M. H., & Nijmeijer, H. (2020). Hybrid integrator-gain systems: A remedy for overshoot limitations in linear control? *IEEE Control Systems Letters*, *4*(4), 1042–1047.

Van den Eijnden, S. J. A. M., Heertjes, M. F., & Nijmeijer, H. (2020). Experimental demonstration of a nonlinear PID-based control design using multiple hybrid integrator-gain elements. In *2020 American control conference* (pp. 4307–4312).

Van den Eijnden, S. J. A. M., Heertjes, M. F., Nijmeijer, H., & Heemels, W. P. M. H. (2024). Stability analysis of hybrid integrator-gain systems: A frequency-domain approach. *Automatica*, *164*, Article 111641.

Van Dinther, D., Sharif, B., Van den Eijnden, S. J. A. M., Nijmeijer, H., Heertjes, M. F., & Heemels, W. P. M. H. (2021). Overcoming performance limitations of linear control with hybrid integrator-gain systems. *IFAC-PapersOnLine*, *54*(5), 289–294.

Van Eijk, L. F., Beer, S., Van Es, R. M. J., Kostić, D., & Nijmeijer, H. (2023). Frequency-domain properties of the hybrid integrator-gain system and its application as a nonlinear lag filter. *IEEE Transactions on Control Systems Technology*, *31*(2), 905–912.

Van Loon, S. J. L. M., Gruntjens, K. G. J., Heertjes, M. F., Van de Wouw, N., & Heemels, W. P. M. H. (2017). Frequency-domain tools for stability analysis of reset control systems. *Automatica*, *82*, 101–108.

Wang, S., Gan, H., Luo, Y., Wang, X., & Chen, Y. (2024). A fractional-order reset ADRC scheme for PMSM speed servo system. In *2024 20th IEEE/aSME international conference on mechatronic and embedded systems and applications* (pp. 1–6). IEEE.

Weekers, W., Kostić, D., Saccon, A., & Van de Wouw, N. (2025). Data-based settling-time optimization for linear feedback control systems using global extremum seeking. *IEEE Transactions on Control Systems Technology*, *33*, 343–353.

Zaccarian, L., Nešić, D., & Teel, A. R. (2005). First order reset elements and the Clegg integrator revisited. In *Proceedings of the 2005 American control conference* (pp. 563–568).

Zames, G. (1981). Feedback and optimal sensitivity: Model reference transformations, multiplicative seminorms, and approximate inverses. *IEEE Transactions on Automatic Control*, *26*(2), 301–320.

Zhao, G., Nešić, D., Tan, Y., & Hua, C. (2019). Overcoming overshoot performance limitations of linear systems with reset control. *Automatica*, *101*, 27–35.